

High-resolution seismic constraints on flow dynamics in the oceanic asthenosphere

Pei-Ying Patty Lin^{1†}, James B. Gaherty¹, Ge Jin¹, John A. Collins², Daniel Lizarralde², Rob. L. Evans² & Greg Hirth³

Convective flow in the mantle and the motions of tectonic plates produce deformation of Earth's interior, and the rock fabric produced by this deformation can be discerned using the anisotropy of the seismic wavespeed^{1–3}. This deformation is commonly inferred close to lithospheric boundaries beneath the ocean in the uppermost mantle, including near seafloor-spreading centres as new plates are formed via corner flow⁴, and within a weak asthenosphere that lubricates large-scale plate-driven flow and accommodates smaller-scale convection^{5,6}. Seismic models of oceanic upper mantle differ as to the relative importance of these deformation processes: seafloor-spreading fabric is very strong just beneath the crust–mantle boundary (the Mohorovičić discontinuity, or Moho) at relatively local scales^{7,8}, but at the global and ocean-basin scales, oceanic lithosphere typically appears weakly anisotropic when compared to the asthenosphere^{9,10}. Here we use Rayleigh waves, recorded across an ocean-bottom seismograph array in the central Pacific Ocean (the NoMelt Experiment), to provide unique localized constraints on seismic anisotropy within the oceanic lithosphere–asthenosphere system in the middle of a plate. We find that azimuthal anisotropy is strongest within the high-seismic-velocity lid, with the fast direction coincident with seafloor spreading. A minimum in the magnitude of azimuthal anisotropy occurs within the middle of the seismic low-velocity zone, and then increases with depth below the weakest portion of the asthenosphere. At no depth does the fast direction correlate with the apparent plate motion. Our results suggest that the highest strain deformation in the shallow oceanic mantle occurs during corner flow at the ridge axis, and via pressure-driven or buoyancy-driven flow within the asthenosphere. Shear associated with motion of the plate over the underlying asthenosphere, if present, is weak compared to these other processes.

The NoMelt experiment was designed to provide localized constraints on the lithosphere–asthenosphere system in a normal oceanic tectonic plate, far from the influence of melting, either at the ridge or due to subsequent intraplate volcanism. NoMelt is centred on mature (70 million years old) Pacific sea floor southeast of Hawaii, between the Clarion and Clipperton fracture zones (Fig. 1). It has an aperture of 600 km × 400 km and consists of a broadband ocean-bottom seismograph (OBS) seismic array, a long-period magnetotelluric survey, and an active-source seismic refraction/reflection survey using a short-period OBS array. The year-long broadband OBS array recorded a large collection of shallow-source earthquakes from around the Pacific basin, and the vertical-component recordings of the Rayleigh surface waves from these events are exceptionally high quality within the period band 20–160 s, once the effects of ocean infragravity waves and tilt noise are removed (see Methods) (Extended Data Fig. 1). By applying ambient-noise interferometry, we extend the Rayleigh-wave observations into a shorter-period (10–20 s) band.

Surface waves traverse NoMelt at a wide range of back-azimuths, providing exceptional azimuthal coverage for estimating shear velocities

and azimuthal anisotropy within the array footprint. We utilize a wide-band intra-array cross-correlation analysis to measure Rayleigh-wave phase velocities in the earthquake band (20–160 s), and a spectral fitting procedure to estimate phase velocity in the ambient-noise band (10–20 s) (see Methods). We find minimal lateral variation in phase velocity within the array, and the observed phase velocities can be expressed by a single, average isotropic phase velocity curve for the entire array, plus a periodic $\cos(2\theta)$ variation in phase velocity as a function of azimuthal direction θ for each frequency (Fig. 2). Such

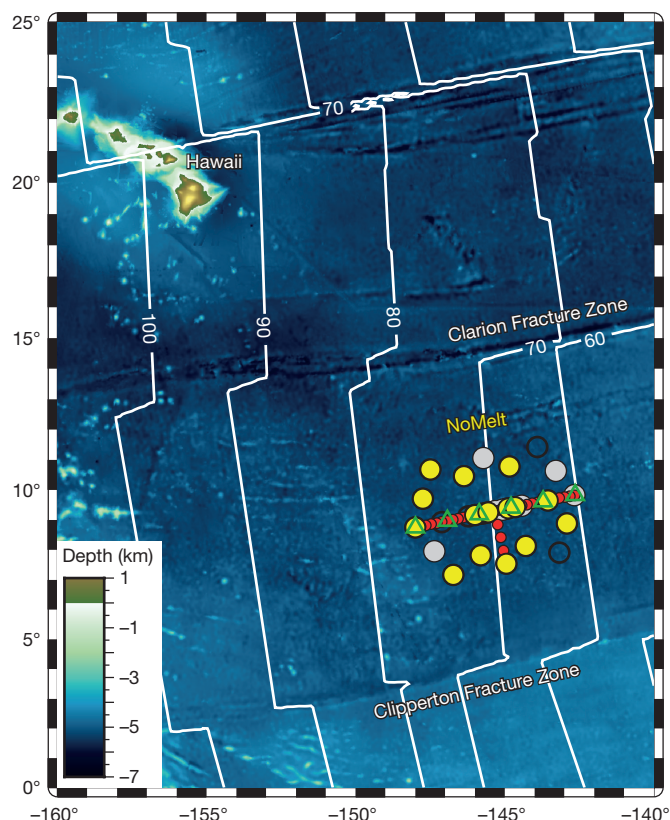


Figure 1 | Layout of NoMelt deployment on a bathymetric map of the central Pacific, with seafloor age (in millions of years) shown as white contours. Solid yellow circles represent broadband OBSs that produced good data; open and grey circles show locations of instruments that were unrecovered or produced poor data, respectively. Red circles and green triangles show locations of short-period OBSs and magnetotelluric instruments, for reference. Seafloor bathymetry was extracted from NOAA (<https://www.ngdc.noaa.gov/mgg/global/global.html>), and the seafloor age is available from EarthByte (http://www.earthbyte.org/Resources/Aggrid/1997/digit_isochrons.html).

¹Lamont-Doherty Earth Observatory of Columbia University, Palisades, New York, USA. ²Department of Geology and Geophysics, Woods Hole Oceanographic Institution, Woods Hole, Massachusetts, USA. ³Geological Sciences Department, Brown University, Providence, Rhode Island, USA. [†]Present address: Taiwan Ocean Research Institute, National Applied Research Laboratories, Kaohsiung, Taiwan (P.-Y.P.L.).

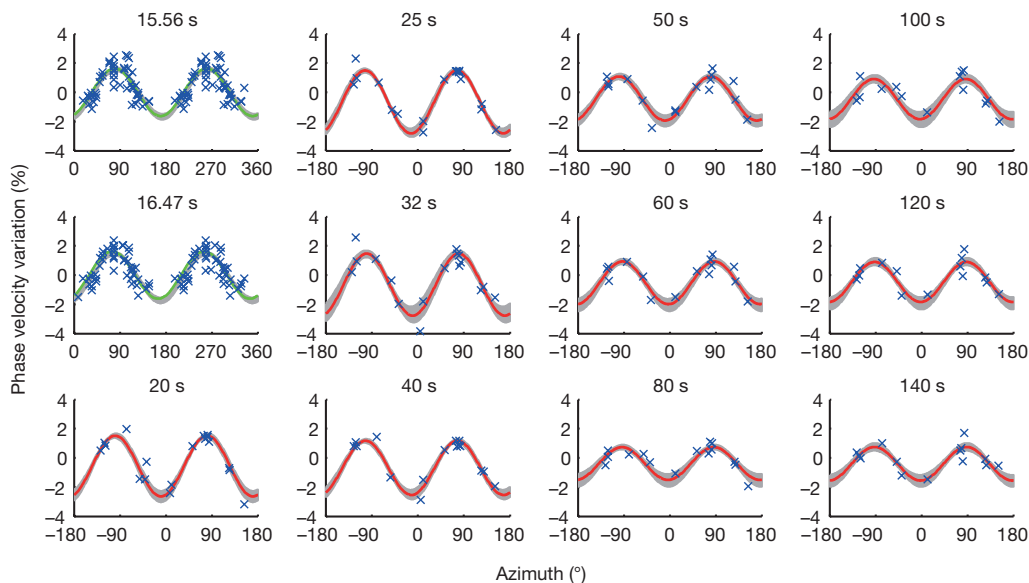


Figure 2 | Examples of the 2θ azimuthal variation of phase velocity measurements at different periods. Blue crosses indicate phase velocity measurements; green and red solid lines are the best-fitting 2θ variation for Rayleigh waves observed from ambient noise and teleseismic events, respectively, with grey bands representing the spread of acceptable 2θ fits as determined by a boot-strap resampling procedure. Period is shown for each panel.

azimuthal anisotropy is diagnostic of deformation-induced olivine fabric in the mantle¹¹, and we observe a very strong peak at $\sim 80^\circ$ azimuth at periods of 14–40 s. The anisotropy appears to weaken at intermediate periods, reaching a minimum at a period of about 80 s before strengthening and rotating slightly towards a more east–west direction at the longest periods (Fig. 2 and insets in Fig. 3b and c).

The average of all the phase velocity dispersion measurements can be inverted to estimate the isotropic one-dimensional vertically polarized shear-velocity structure (V_{sv}) beneath the array. We utilize an iterative, linearized least-squares inversion algorithm, with an additional Monte Carlo scheme to evaluate uncertainty associated with choice of starting model. The best-fitting V_{sv} profiles (Fig. 3a) are characterized by a thin high-velocity lid overlying a modest low-velocity zone, similar to other local and/or regional models of the Pacific^{12,13}. The absolute velocities in both the lid and the low-velocity zone, as well as the transition between them (50–80 km depth), are very tightly constrained owing to the small uncertainty in the average phase velocity observations. The inferred seismic velocities are consistent with electrical conductivity profiles that suggest a dry lid overlying a modestly damp asthenosphere at subsolidus temperatures¹⁴—no melt appears to be required to produce either the low-velocity zone¹⁵ or the high-conductivity zone¹⁴, although very small amounts of melt cannot be ruled out. Regardless of melt content, the rheological profile across the system should correlate strongly with the shear-velocity profile, with a minimum in viscosity that coincides roughly with the middle of the low-velocity zone¹⁶.

We invert the frequency-dependent $\cos(2\theta)$ variations in phase velocity for 2θ models of azimuthal anisotropy (the G parameter) as a function of depth (Fig. 3b and c) using a smooth parameterization and a linearized least-squares algorithm (see Methods). The best-fitting models show the strongest anisotropy in the lithosphere with the fast direction parallel to the fossilized (dating to plate formation) seafloor-spreading direction (78°) estimated from the orientation of nearby fracture zones, and then decreasing in magnitude with depth into the asthenosphere. The weakest azimuthal anisotropy is centred in the asthenosphere at 100–150 km depth, and then it increases to a secondary maximum at about 250 km depth. Fast directions rotate modestly from the fossil-spreading direction within the lithosphere to a more east–west direction at depth. The data provide clear evidence for this basic layered structure (insets to Fig. 3b and c): strong G anisotropy at the Moho is driven by the peak in azimuthal velocity variations near 20-s period; the decay in G amplitude is required by the steep reduction in azimuthal variation in the period band 20–50 s; the secondary maximum in G amplitude near 250 km depth is required by the persistence of peak-to-peak azimuthal variations of $\sim 3\%$ out to the longest period; and the rotation in G azimuth with depth in the mantle is required by

the rotation of the fast propagation direction from $\sim 75^\circ$ to $\sim 90^\circ$ across the period band 50–140 s. The preferred models are not consistent with anisotropy in the asthenosphere aligned with apparent plate motion (APM) in a hotspot reference frame (Fig. 3c).

The models of azimuthal anisotropy have several key implications for the nature of deformation and flow associated with oceanic tectonic plates. First, corner flow at the mid-ocean ridge represents the dominant fabric-forming process in the shallow oceanic mantle. This mechanism has long been recognized as important for explaining olivine fabric observed in ophiolites¹⁷ and abyssal peridotites¹⁸ and the presumably related seismic anisotropy observed in the oceanic lithosphere¹, particularly at the shallow depths constrained by active-source seismic refraction experiments^{7,8,19}. Our results suggest that this fabric extends down at least 50 km into the cooling plate, providing new constraints on models of ridge dynamics⁴. The strength of this anisotropy is noticeably greater than that associated with deformation in the underlying asthenosphere. This high-resolution result is at odds with Pacific-wide studies of seismic anisotropy, which argue for a weakly anisotropic lithosphere underlain by a highly anisotropic asthenosphere^{9,20}. This difference probably reflects the limited ability of large-scale studies to resolve structure imparted by seafloor spreading²¹, which exhibits lateral heterogeneity over short length scales, as compared to larger-scale processes such as apparent plate motion or density-driven flow^{22,23}.

Below the plate, our results suggest that the strongest deformation is induced by dynamic flow within the asthenosphere, rather than passive shear strain associated with motion of the plate over the underlying mantle. This conclusion is supported by the absence of an APM signal and by the pattern of anisotropic strength with depth: the fast anisotropic direction does not align with APM within any depth interval, and the anisotropy is weakest near the base of the plate, where APM-induced strain should accumulate, and peaks near 250 km depth, deep in the asthenosphere, consistent with deformation caused by dynamic flow. Although our results strongly favour asthenospheric flow as the source of the observed anisotropic signal beneath the plate, we cannot directly constrain the details of this flow. This is because the apparent fast directions correspond to differential shear between plate flow, flow within the asthenosphere, and flow within the subasthenospheric mantle²⁴—the former is known, but the latter two are not. This ambiguity exists for the case of shear flow with length scales larger than the 400-km array, and for deformation processes with length scales smaller than the NoMelt array, where the azimuthal signal will additionally include averages of local fabric variations.

The lack of an APM signal in our high-resolution study contrasts sharply with most large-scale studies of the Pacific mantle^{9–11,20}. The

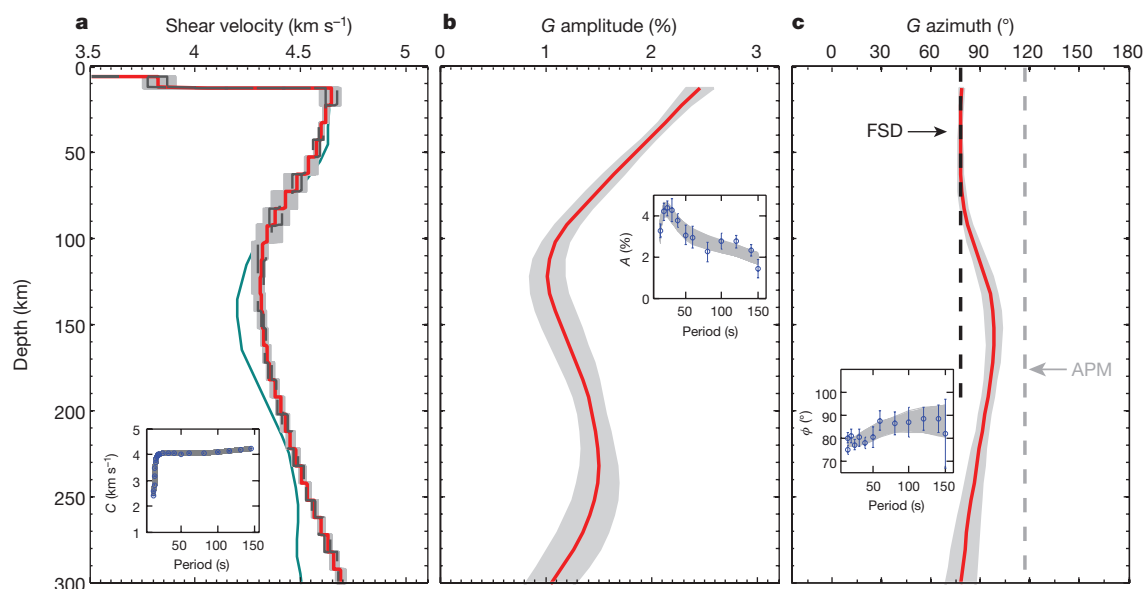


Figure 3 | Shear velocity and azimuthal anisotropy models in the upper mantle beneath NoMelt. **a**, The grey band depicts the span of shear velocity models resulting from inversion using 100 distinct starting models; the mean shear velocity model and associated standard deviation (s.d.) are shown by the solid red line and dashed black line, respectively. The blue line is a 52–110-million-year-old Pacific model¹³ as a reference. The inset shows the phase velocities (C , calculated on the basis of the inverted shear velocity models; grey lines) compared to the observations (blue circles with 1 s.d.). **b**, The modelled strength of azimuthal anisotropy

is shown by the solid red line with the grey shading showing ± 1 s.d. from 1,000 randomly generated resamplings of the observed measurements. The inset shows the predicted peak-to-peak amplitude (A ; grey lines) compared to the observations (blue circles with error bars of 1 s.d.). **c**, As for **b** but showing the direction of the azimuthal anisotropy. The vertical black and grey dashed lines indicate the orientation of fossil spread direction (FSD) and apparent plate motion (APM)³³. The inset shows the predicted fast direction (ϕ ; grey lines) compared to the observations (blue circles with error bars of 1 s.d.).

difference between our inferred fast directions and that predicted by APM is robust and statistically significant (see Methods). The discrepancy between our result and previous models probably arises due to the averaging inherent in seismic tomography; the amplitude of the largest-scale structures is recovered, whereas the strength of smaller-scale structures is underestimated if they are poorly resolved. APM is coherent at the scale of the entire Pacific plate, and this may explain why it is so prominent in Pacific-scale tomographic models. In detail, a few plate-scale models show subtle non-APM variations in the NoMelt region³, and some authors prefer alternative flow processes to APM even at the plate scale²³. Our result demonstrates that the smaller-scale processes of corner flow and asthenospheric dynamics are

regionally more dominant than APM in controlling the development and evolution of seismic anisotropy in the mantle beneath the oceans.

The pattern (or structure) of anisotropy with depth suggests two scenarios for the dominant geodynamic flow in the central Pacific asthenosphere. Both scenarios hypothesize a low-viscosity asthenospheric channel^{5,25}, with the viscosity within the channel described by a power-law rheology. Large-scale pressure gradients within the asthenosphere would induce Poiseuille flow with a plug-like velocity profile (Fig. 4a). In such flow, fabric-inducing strain gradients are localized near the top and bottom boundaries of the channel, with relatively little fabric produced in the centre of the system; this scenario nicely matches the anisotropy–strength profile observed beneath NoMelt. Anisotropy

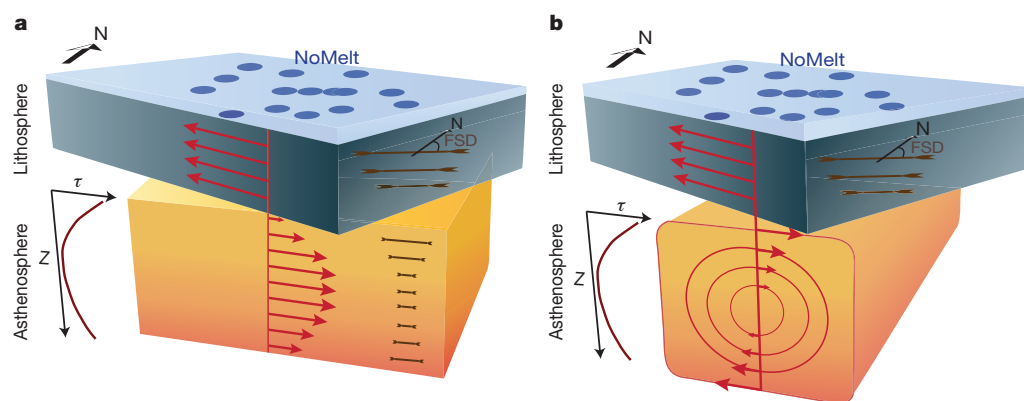


Figure 4 | Schematic of proposed models for azimuthal anisotropy beneath the NoMelt experiment. **a**, **b**, Pressure-gradient-driven flow (**a**) and density-driven small-scale convection (**b**) in the asthenosphere. At the top is the surface view; black arrows show the direction of north, with circles denoting NoMelt broadband OBSs. The red arrows indicate the flow direction in the lithosphere–asthenosphere system. The lithosphere moves at plate velocity at all depths. The direction of dynamic flow in the asthenosphere is shown as roughly east-to-west, as obtained from our azimuthal anisotropy model. The anisotropy signals in the lithosphere

are frozen rock fabric (shown as brown segments) imparted by shear strain during corner flow at the ridge axis. Anisotropic strength in the lithosphere is largest at the top, decreases with depth, and is oriented with the FSD. The shear-strain gradient (maroon curve; Z , depth; τ , shear strain) resulting from dynamic flow is largest at the top and the base of the asthenosphere and smallest in the mid-asthenosphere for flow driven by either pressure gradients or density, producing rock fabric as indicated by the brown segments.

associated with the top boundary is difficult to distinguish from the lithospheric fabric, but the peak near 250 km depth would represent a shear zone at the lower boundary of the channel. Thermally induced pressure gradients within the asthenosphere may be associated with several geodynamic phenomena, including return flow from subduction zone to mid-ocean ridge²⁶, ridge-induced flow beneath the oceanic plates²⁷, and, more generally, density-driven flow^{22,23}. Assuming a static upper mantle beneath the asthenosphere, the apparent east–west fast direction of anisotropy in the lower asthenosphere is generally consistent with the first two scenarios. That is, ridge-driven flow would be approximately east–west, while return flow would be west–east. Published density-driven flow models do not predict east–west asthenospheric flow in the NoMelt region²³ so the observations presented here should prove useful in refining future models.

Alternatively, density-driven small-scale convection within the low-viscosity channel could also produce fabric consistent with the anisotropy observations (Fig. 4b). In this scenario, horizontal flow at the top and bottom of convection cells produces strong azimuthal anisotropy for surface waves, while the centre of the channel exhibits weak and/or quasi-vertical fabric that results in little detectable azimuthal anisotropy, especially if the convection is on a length scale smaller than the array. Small-scale convection has long been invoked to explain bathymetry²⁸ and gravity observations²⁹ in the Pacific, most specifically in the form of organized thermal instabilities (“Richter Rolls”³⁰) beneath the base of the plate. Direct observations of such structures in the asthenosphere have proved elusive³¹, and our observation of east–west fabric is not consistent with the traditional Richter-Roll mechanism, which predicts horizontal fabric orthogonal to the APM-oriented long axis of the rolls. However, a recent high-resolution gravity compilation³² reveals gravity lineations with orientations that vary over length scales of several hundred kilometres, perhaps indicating that small-scale convection beneath the Pacific is more three-dimensional than the traditionally invoked mechanism. Our observations may place direct constraints on the localized orientation of small-scale convection within the NoMelt region.

Online Content Methods, along with any additional Extended Data display items and Source Data, are available in the online version of the paper; references unique to these sections appear only in the online paper.

Received 29 October 2015; accepted 13 April 2016.

Published online 6 July 2016.

- Hess, H. H. Seismic anisotropy of the uppermost mantle under oceans. *Nature* **203**, 629–631 (1964).
- Forsyth, D. W. The early structural evolution and anisotropy of the oceanic upper mantle. *Geophys. J. Int.* **43**, 103–162 (1975).
- Montagner, J. P. Upper mantle low anisotropy channels below the Pacific Plate. *Earth Planet. Sci. Lett.* **202**, 263–274 (2002).
- Blackman, D. K. & Kendall, J. M. Seismic anisotropy in the upper mantle 2. Predictions for current plate boundary flow models. *Geochem. Geophys. Geosyst.* **3**, 8602 (2002).
- Phipps Morgan, J., Morgan, W. J., Zhang, Y.-S. & Smith, W. H. F. Observational hints for a plume-fed, suboceanic asthenosphere and its role in mantle convection. *J. Geophys. Res.* **100**, 12753–12767 (1995).
- Agrusta, R. *et al.* Small-scale convection in a plume-fed low-viscosity layer beneath a moving plate. *Geophys. J. Int.* **194**, 591–610 (2013).
- Raitt, R. W., Shor, G. G., Francis, T. J. G. & Morris, G. B. Anisotropy of the Pacific upper mantle. *J. Geophys. Res. Solid Earth* **74**, 3095–3109 (1969).
- Gaherty, J. B., Lizarralde, D., Collins, J. A., Hirth, G. & Kim, S. Mantle deformation during slow seafloor spreading constrained by observations of seismic anisotropy in the western Atlantic. *Earth Planet. Sci. Lett.* **228**, 255–265 (2004).
- Beghein, C., Yuan, K., Schmerr, N. & Xing, Z. Changes in seismic anisotropy shed light on the nature of the Gutenberg discontinuity. *Science* **343**, 1237–1240 (2014).
- Burgos, G. *et al.* Oceanic lithosphere–asthenosphere boundary from surface wave dispersion data. *J. Geophys. Res. Solid Earth* **119**, 1079–1093 (2014).
- Montagner, J.-P. & Nataf, H.-C. Vectorial tomography—I. Theory. *Geophys. J. Int.* **94**, 295–307 (1988).

- Tan, Y. & Helmberger, D. V. Trans-Pacific upper mantle shear velocity structure. *J. Geophys. Res.* **112**, B08301 (2007).
- Nishimura, C. E. & Forsyth, D. W. The anisotropic structure of the upper mantle in the Pacific. *Geophys. J. Int.* **96**, 203–229 (1989).
- Sarafian, E. *et al.* The electrical structure of the central Pacific upper mantle constrained by the NoMelt experiment. *Geochem. Geophys. Geosyst.* **16**, 1115–1132 (2015).
- Jackson, I. & Faul, U. H. Grainsize-sensitive viscoelastic relaxation in olivine: towards a robust laboratory-based model for seismological application. *Phys. Earth Planet. Inter.* **183**, 151–163 (2010).
- Hirth, G. & Kohlstedt, D. L. Water in the oceanic upper mantle: implications for rheology, melt extraction and the evolution of the lithosphere. *Earth Planet. Sci. Lett.* **144**, 93–108 (1996).
- Nicolas, A., Ceuleneer, G., Boudier, F. & Misseri, M. Structural mapping in the Oman ophiolites: mantle diapirism along an oceanic ridge. *Tectonophysics* **151**, 27–56 (1988).
- Ismail, W. B. & Mainprice, D. An olivine fabric database: an overview of upper mantle fabrics and seismic anisotropy. *Tectonophysics* **296**, 145–157 (1998).
- Shearer, P. & Orcutt, J. Anisotropy in the oceanic lithosphere — theory and observations from the Ngendei seismic refraction experiment in the south-west Pacific. *Geophys. J. R. Astron. Soc.* **80**, 493–526 (1985).
- Maggi, A., Debayle, E., Priestley, K. & Barruol, G. Azimuthal anisotropy of the Pacific region. *Earth Planet. Sci. Lett.* **250**, 53–71 (2006).
- Debayle, E. & Ricard, Y. Seismic observations of large-scale deformation at the bottom of fast-moving plates. *Earth Planet. Sci. Lett.* **376**, 165–177 (2013).
- Conrad, C. P. & Behn, M. D. Constraints on lithosphere net rotation and asthenospheric viscosity from global mantle flow models and seismic anisotropy. *Geochem. Geophys. Geosyst.* **11**, Q05W05 (2010).
- Becker, T. W., Conrad, C. P., Schaeffer, A. J. & Lebedev, S. Origin of azimuthal seismic anisotropy in oceanic plates and mantle. *Earth Planet. Sci. Lett.* **401**, 236–250 (2014).
- Silver, P. G. & Holt, W. E. The mantle flow field beneath western North America. *Science* **295**, 1054–1057 (2002).
- Becker, T. W. On the effect of temperature and strain-rate dependent viscosity on global mantle flow, net rotation, and plate-driving forces. *Geophys. J. Int.* **167**, 943–957 (2006).
- Buck, W. R., Small, C. & Ryan, W. B. F. Constraints on asthenospheric flow from the depths of oceanic spreading centers: the East Pacific Rise and the Australian–Antarctic discordance. *Geochem. Geophys. Geosyst.* **10**, Q09007 (2009).
- Höink, T., Lenardic, A. & Richards, M. Depth-dependent viscosity and mantle stress amplification: implications for the role of the asthenosphere in maintaining plate tectonics. *Geophys. J. Int.* **191**, 30–41 (2012).
- Parsons, B. & McKenzie, D. Mantle convection and the thermal structure of the plates. *J. Geophys. Res. Solid Earth* **83**, 4485–4496 (1978).
- Haxby, W. F. & Weissel, J. K. Evidence for small-scale mantle convection from Seasat altimeter data. *J. Geophys. Res. Solid Earth* **91**, 3507–3520 (1986).
- Richter, F. M. & Parsons, B. On the interaction of two scales of convection in the mantle. *J. Geophys. Res. Solid Earth* **80**, 2529–2541 (1975).
- French, S., Lekic, V. & Romanowicz, B. Waveform tomography reveals channelled flow at the base of the oceanic asthenosphere. *Science* **342**, 227–230 (2013).
- Sandwell, D. T., Müller, R. D., Smith, W. H. F., Garcia, E. & Francis, R. New global marine gravity model from CryoSat-2 and Jason-1 reveals buried tectonic structure. *Science* **346**, 65–67 (2014).
- Argus, D. F. & Gordon, R. G. No-net-rotation model of current plate velocities incorporating plate motion model NUVEL-1. *Geophys. Res. Lett.* **18**, 2039–2042 (1991).

Acknowledgements We thank the scientific party, captain, crews, and technical teams of RV *Marcus G. Langseth* and RV *Melville* for work that made this study possible. The OBS were provided and supported by Scripps Institution of Oceanography’s facility as part of the US Ocean Bottom Seismograph Instrument Pool (<http://www.obsip.org>). This work was funded by the US National Science Foundation. P.-Y.P.L. thanks the Institute of Earth Science, Academia Sinica, Taipei, Taiwan and Institute of Undersea Technology, National Sun Yat-sen University, Kaohsiung, Taiwan for support during completion of this work.

Author Contributions P.-Y.P.L. and J.B.G. collaborated in developing the concept of this paper and writing the first draft. All authors contributed to the scientific discussion, including presentation of results, interpretation, and implications.

Author Information Reprints and permissions information is available at www.nature.com/reprints. The authors declare no competing financial interests. Readers are welcome to comment on the online version of the paper. Correspondence and requests for materials should be addressed to P.-Y.P.L. (pylin.patty@gmail.com).

METHODS

Tilt and compliance noise correction for OBS vertical-component data. OBS data often contain substantial noise sources that are not present in land-based seismic records. OBS vertical data are contaminated by compliance noise induced by infragravity waves that are also recorded on bottom-pressure data³⁴, and tilt noise induced by bottom currents that leaks from horizontal components³⁵. We calculate spectral transfer functions between pressure-vertical and horizontal-vertical component data, and apply this transfer function to the vertical components to remove the compliance and tilt noise. At this location and water depth (about 5,200 m), the coherent tilt noise is usually modest, and results in a subtle reduction in noise at periods longer than about 60 s (Extended Data Fig. 1). The compliance signal is quite strong, but is limited to periods longer than about 90 s, and after correction the noise levels of vertical data decrease substantially at long periods. Owing to possible spatial and temporal variation in noise characteristics, the transfer functions of each station are determined for each event individually³⁶. To construct the transfer functions, we calculated the spectra and coherence of all pairs of vertical- and horizontal-component seismic data, and differential-pressure data, for two days before each event recording. The two-day-long seismogram was cut into 40 overlapping time windows of length 6,000 s, and spectra, coherence, and transfer functions were calculated and applied as described by refs 1 and 2.

Phase velocity analysis. At long periods (20–150 s), we estimate phase velocities within the array by applying the Automated Surface-Wave Measuring System³⁷ on Rayleigh waveforms (Extended Data Fig. 2a) of 19 teleseismic earthquakes with moment magnitude over 6.5 (Extended Data Fig. 3). Frequency-dependent phase delays between pairs of nearby stations are measured using cross correlation; the phase delays are then inverted for phase velocities via the Eikonal equation³⁸. Lateral variations in phase velocities are small, and we utilize the dispersion in the centre of the array for each event to characterize average structure within the array. The measured phase velocities are strongly dependent on station-to-source azimuth, and at each frequency we solve for the azimuthally averaged phase velocity, plus the magnitude and direction of azimuthal variations of the form $\cos(2\theta) + \cos(4\theta)$, where θ represents azimuth from the centre of the array³⁹.

We apply the ambient-noise cross-correlation technique to obtain the phase velocities at short periods (10–20 s). The cross-correlation spectra are stacked to retrieve surface-wave Green's functions between station pairs (Extended Data Fig. 2b), and the frequency-dependent phase velocity curve for each station-to-station path is estimated by fitting the cross-spectra⁴⁰. These inter-station dispersion curves are inverted for azimuthally averaged phase velocity plus $\cos(2\theta) + \cos(4\theta)$ variations at each frequency. While we include 4θ terms for the azimuthal variations in both ambient noise and earthquake observations, the amplitude of these terms is very small for all periods (0.09% to 0.4%), and the changes to the 2θ terms is indistinguishable. *F*-test calculations suggest that these estimates of azimuthal anisotropy do not substantially improve the fit to the data when compared to models including only 2θ variation, so we utilize the 2θ -only estimates to invert for azimuthally anisotropic velocity structure. We use a bootstrap resampling algorithm to test the robustness and stability of the 2θ estimates at each frequency; the error bars on the observations (Fig. 3 and Extended Data Fig. 4) conservatively include the formal errors of the misfit, as well as the potential variance inferred from the bootstrap analysis.

Inversion for azimuthally anisotropic shear velocity. The azimuthally averaged phase velocity dispersion curve is used to estimate a shear-velocity profile as a function of depth via linearized least-squares inversion⁴¹. We calculate a set of acceptable one-dimensional V_{sv} models using a set of 100 starting models. The 2θ azimuthal dependence can be expressed as combinations of the elastic parameters of B , H and G (ref. 42), with the Rayleigh waves dominated by the parameters for G (ref. 43). In this study, we then modelled the $\cos(2\theta)$ azimuthal variations in phase velocity by using combinations of the depth-dependent parameters G_c and G_s , where the subscripts c and s denote cosine and sine azimuthal dependence⁴⁴. The amplitude and azimuth of G as a function of depth can be computed as $\sqrt{G_c^2 + G_s^2}$ and $0.5 \tan^{-1} \frac{G_s}{G_c}$, respectively.

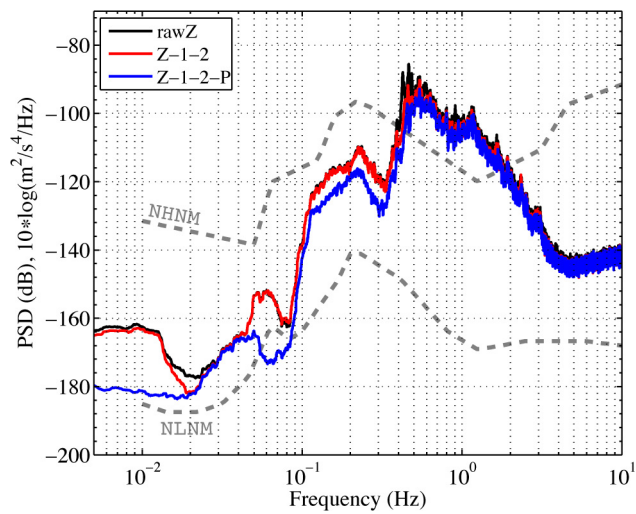
The observed peak-to-peak amplitude A and fast direction ϕ as a function of period can be used to define the data parameters D_c and D_s , where the subscripts c and s denote cosine and sine fast-direction dependence: $D_c = A \cos 2\phi$ and $D_s = A \sin 2\phi$.

The kernels that relate the data parameters D_c and D_s to model parameters and can be assumed to be the same down to a depth of 500 km as $L = \rho V_{sv}^2$ (ref. 44). We use the average of the best-fitting V_{sv} model determined from the average dispersion curve for the kernel calculation in the azimuthal inversion. We invert for G_c and G_s with a smooth parameterization and a linearized least-squares algorithm that minimizes misfit of D_c and D_s (ref. 42).

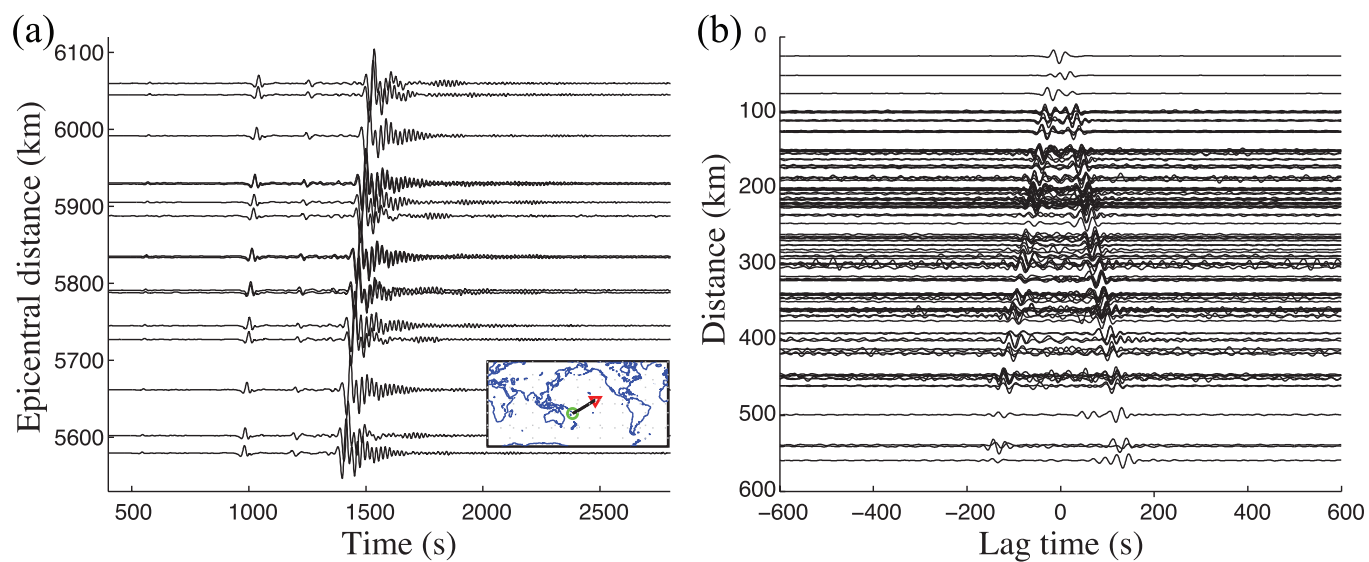
Forward calculations. We utilize forward modelling to explicitly test the robustness of three key characteristics of the inverted anisotropy models (Extended Data Fig. 4). First, we test for the necessity of the secondary peak in anisotropy deep in the asthenosphere. This feature is required to explain the persistent strong azimuthal signal observed in phase velocity at periods of 90 s and longer. Squeezing tests suggest that this structure probably persists to at least 300 km; restricting it to smaller depth maintains a peak in amplitude near 200–250 km, with the amplitude of the peak increasing dramatically as the depth distribution is pushed to depths of <300 km. Second, we test for the possibility of the smoother models for the strength and the direction of the anisotropy (orange solid lines) that specifically do not have a minimum of amplitude in the asthenosphere. Owing to the weakening in the observed strength of the peak-to-peak velocity variations between periods of 30–60 s, the smoother model without a notch in amplitude near a depth of 120 km does not fit the decaying pattern in G amplitude. Third, we evaluate whether a layer of asthenospheric anisotropy parallel to apparent plate motion (APM) might be unresolved by our surface-wave data. Such anisotropy is often inferred at the base of the plate^{9,23}. We find that, if present, APM anisotropy must be weak (<1%) and within a layer of thickness <20 km to satisfy the observed fast-direction observations at periods of 40 s and greater within the observational uncertainties.

Code availability. NoMelt data has been archived under network code ZA at the IRIS Data Management Center (<http://ds.iris.edu/gmap/ZA?timewindow=2011-2013>). Software for array analysis of surface waves is available at <https://ds.iris.edu/ds/products/aswms/>.

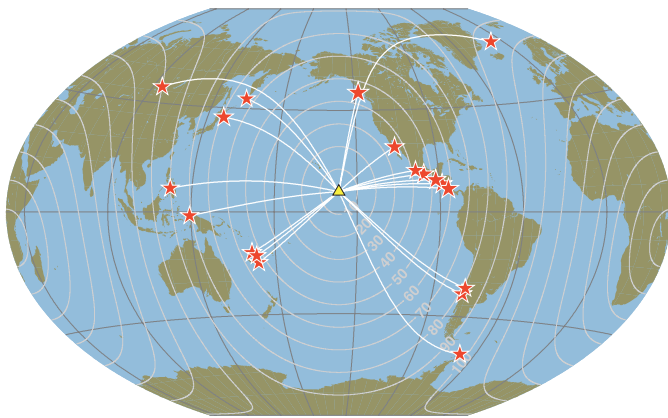
34. Webb, S. C. & Crawford, W. C. Long-period seafloor seismology and deformation under ocean waves. *Bull. Seismol. Soc. Am.* **89**, 1535–1542 (1999).
35. Crawford, W. C. & Webb, S. C. Identifying and removing tilt noise from low-frequency (<0.1 Hz) seafloor vertical seismic data. *Bull. Seismol. Soc. Am.* **90**, 952–963 (2000).
36. Bell, S. W., Forsyth, D. W. & Ruan, Y. Removing noise from the vertical component records of ocean-bottom seismometers: results from year one of the Cascadia Initiative. *Bull. Seismol. Soc. Am.* **105**, 300–313 (2015).
37. Jin, G. & Gaherty, J. B. Surface wave phase-velocity tomography based on multichannel cross-correlation. *Geophys. J. Int.* **201**, 1383–1398 (2015).
38. Lin, F.-C., Ritzwoller, M. H. & Snieder, R. Eikonal tomography: surface wave tomography by phase front tracking across a regional broad-band seismic array. *Geophys. J. Int.* **177**, 1091–1110 (2009).
39. Smith, M. L. & Dahlen, F. A. The azimuthal dependence of Love and Rayleigh wave propagation in a slightly anisotropic medium. *J. Geophys. Res. Solid Earth* **78**, 3321–3333 (1973).
40. Menke, W. & Jin, G. Waveform fitting of cross spectra to determine phase velocity using Aki's formula. *Bull. Seismol. Soc. Am.* **105**, 1619–1627 (2015).
41. Herrmann, R. B. Computer programs in seismology: an evolving tool for instruction and research. *Seismol. Res. Lett.* **84**, 1081–1088 (2013).
42. Montagner, J.-P. & Nataf, H.-C. A simple method for inverting the azimuthal anisotropy of surface waves. *J. Geophys. Res. Solid Earth* **91**, 511–520 (1986).
43. Zhu, H. & Tromp, J. Mapping tectonic deformation in the crust and upper mantle beneath Europe and the North Atlantic Ocean. *Science* **341**, 871–875 (2013).
44. Montagner, J. P. & Tanimoto, T. Global upper mantle tomography of seismic velocities and anisotropies. *J. Geophys. Res.* **96**, 20337–20351 (1991).
45. Peterson, J. *Observation and modeling of seismic background noise*. Open-File Report No. 93-322 (US Department of Interior Geological Survey, 1993).



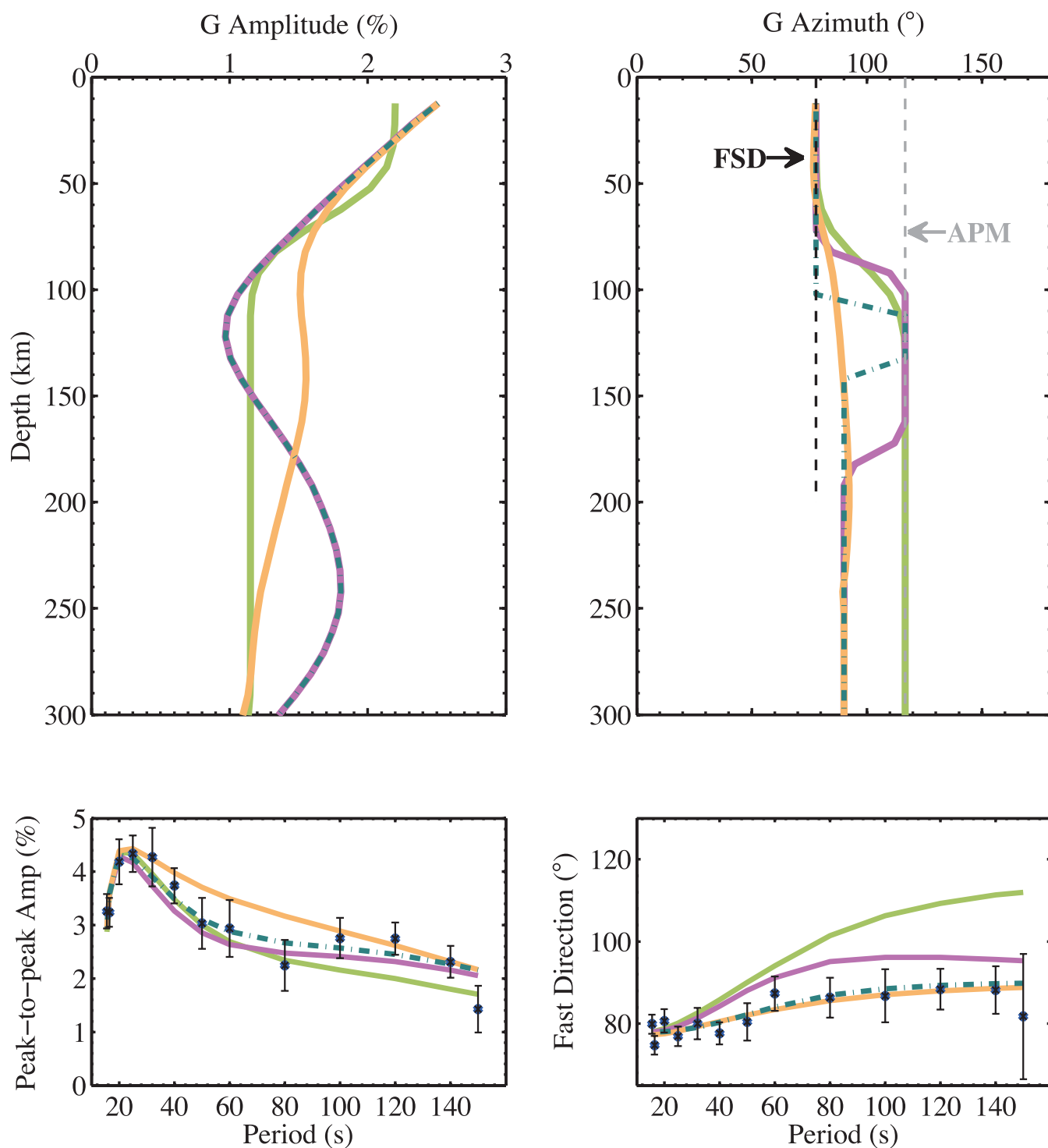
Extended Data Figure 1 | Power spectral densities (PSDs) of raw, tilt and compliance noise-removed seismograms. The PSD values are calculated from vertical data recorded by one NoMelt station, B13, located at 9.25° N, 145.55° W). The black curves show the spectrum of the raw vertical component. The red and blue curves show the spectrum after removing the tilt noise and compliance noise, respectively. The PSD is reported in decibels (dB) referenced to $10\log[\text{AAS} (\text{m}^{-2} \text{s}^{-4} \text{Hz}^{-1})]$, where AAS is the acceleration-amplitude spectrum. The new high- and low-noise models of ref. 45, NHNM and NLNM (thin dashed lines), are shown as references.



Extended Data Figure 2 | Rayleigh waveforms recorded by NoMelt. **a**, Broadband vertical-component seismograms filtered in the 20–100-s period band from an event (green circle) in the southwestern Pacific (see inset map). The red inverted triangle denotes the NoMelt location. **b**, Ambient noise cross-correlation waveforms, filtered between 10 s and 25 s in the time domain.



Extended Data Figure 3 | Shallow-telesismic event distribution. 19 events (red stars) with high-quality Rayleigh waves were recorded during NoMelt one-year deployment. White lines represent the corresponding great-circle paths. Grey contours show the epicentral distances at 10° intervals.



Extended Data Figure 4 | Forward calculations. The upper panels show four input models of G parameters (green solid, magenta solid, orange solid and blue dashed-dotted lines). The lower panels show the forward-calculated peak-to-peak amplitude A and fast direction ϕ as functions of

period from the four models. Our observations are shown as blue circle symbols with error bars of 1 s.d. as references. The black and grey dashed lines indicate the orientation of the FSD and apparent plate motion (APM) at the NoMelt location.